ACS APPLIED MATERIALS & INTERFACES

Research Article

www.acsami.org

Enhanced *In Vitro* and *In Vivo* Cellular Imaging with Green Tea Coated Water-Soluble Iron Oxide Nanocrystals

Lisong Xiao,[†] Marianne Mertens,[‡] Laura Wortmann,[†] Silke Kremer,[†] Martin Valldor,[§] Twan Lammers,[‡] Fabian Kiessling,[‡] and Sanjay Mathur*[,†,#]

[†]Institute of Inorganic Chemistry, University of Cologne, D-50939 Cologne, Germany

[‡]Department of Experimental Molecular Imaging, RWTH Aachen University Hospital, D-52074 Aachen, Germany

[§]Max-Planck-Institute for Chemical Physics and Solids, D-01187 Dresden, Germany

[#]International Research Center for Renewable Energy, School of Energy & Power Engineering, Xian Jiaotong University, Xian (Shaanxi) 710049, PR China

Supporting Information

ABSTRACT: Fully green and facile redox chemistry involving reduction of colloidal iron hydroxide ($Fe(OH)_3$) through green tea (**GT**) polyphenols produced water-soluble Fe_3O_4 nanocrystals coated with **GT** extracts namely epigallocatechin gallate (**EGCG**) and epicatechin (**EC**). Electron donating polyphenols stoichiometrically reduced Fe^{3+} ions into Fe^{2+} ions resulting in the formation of magnetite (Fe_3O_4) nanoparticles and corresponding oxidized products (semiquinones and quinones) that simultaneously served as efficient surface chelators for the Fe_3O_4 nanoparticles making them dispersible and stable in water, PBS, and cell culture medium for extended time periods. As-formed iron oxide nanoparticles (2.5−6 nm) displayed high crystallinity and saturation magnetization as well as high relaxivity ratios manifested in strong contrast enhancement observed in T_2-weighted images. Potential of green tea-coated superparamagnetic iron oxide nanocrystals (SPIONs) as superior negative contrast agents was confirmed by *in vitro* and *in vivo* experiments. Primary human macrophages (J774A.1) and colon cancer cells (CT26) were chosen to assess cytotoxicity and cellular uptake of **GT**-, **EGCGq**-, and **ECq**-coated Fe_3O_4 nanoparticles, which showed high uptake efficiencies by J774A.1 and CT26 cells without any additional transfection agent. Furthermore, the in vivo accumulation characteristics of **GT**-coated Fe_3O_4 nanoparticles were similar to those observed in clinical studies of SPIONs with comparable accumulation in epidermoid cancer-xenograft bearing mice. Given their promising transport and uptake characteristics and new surface chemistry, **GT-SPIONs** conjugates can be applied for multimodal imaging and therapeutic applications by anchoring further functionalities.

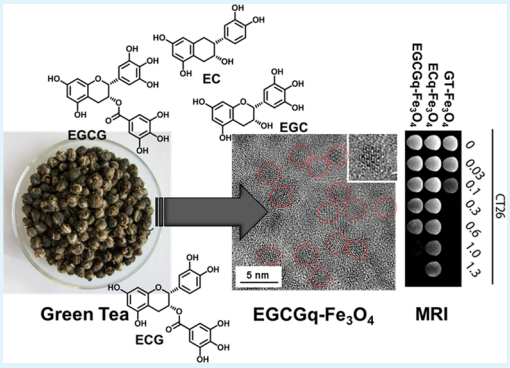

KEYWORDS: *superparamagnetic carriers, iron oxide nanoparticles, magnetic resonance imaging (MRI), biocompatible probes, green tea catechins*

INTRODUCTION

Nanoscopic carriers for cellular applications have emerged as a critically important class of nanomaterials for biomedical technology, particularly due to their favorable magnetic properties, low toxicity, and high chemical stability under physiological conditions.[1−4] Superparamagnetic iron oxide nanoparticles (SPIONs) are useful T_2 contrast agent for magnetic resonance imaging (MRI) applied in clinical diagnosis especially because of higher spatial resolution and enhanced contrast in soft tissues than other imaging modalities.[5−7] Recent advances in nanotechnology have demonstrated size-dependent uptake and removal of nanoparticles making them interesting carriers for therapeutic and diagnostic cargos.[8] In this context, tremendous efforts have been made to develop SPIONs as viable MRI contrast agents by enhancing their colloidal stability and transport efficacy by attaching biocompatible and biodegradable surface groups.[8,9] Typically, iron oxide nanoparticles are synthesized either by coprecipitation,[10,11] or high-temperature decomposition of metal−organic iron precursors[12−16] in suitable solvents.[17−20] The preferred method for iron oxide nanoparticles is generally chosen based on the simplicity and scaling-up potential of the synthesis procedure together with a strict control over the particle size in the final material. For a straightforward and scalable synthesis of water-soluble FeO_x quantum dots, coprecipitation of Fe(II) and Fe(III)-hydroxides in aqueous solution appears to be an obvious choice. However, coprecipitation reactions do not offer good control over reaction kinetics, as often manifested in broad size-distribution, low crystallinity and coexistence of different Fe:O stoichiometries in the resulting SPIONs.[11,21]

Received: December 1, 2014
Accepted: March 2, 2015
Published: March 2, 2015

DOI: 10.1021/am508404t
ACS Appl. Mater. Interfaces 2015, 7, 6530−6540

Scheme 1. Schematic Representation for the Preparation Strategy for (A) ECq-Fe_3O_4 and (B) EGCGq-Fe_3O_4 NPs[a]

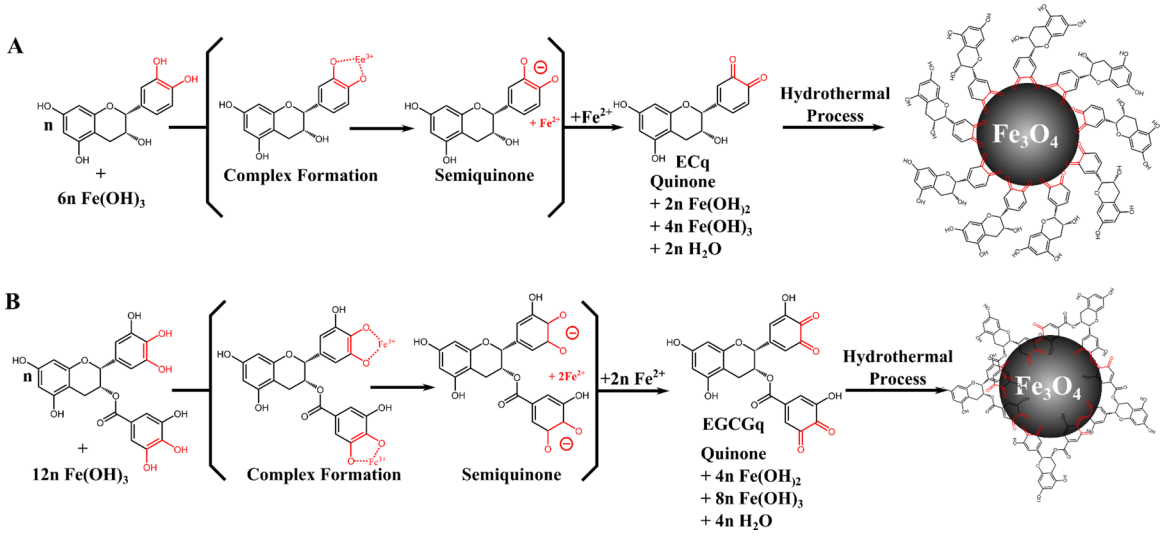

[a]The reaction mechanism for the formation of **GT**-Fe_3O_4 is following the same schematic pathway except that **EC** or **EGCG** is replaced by a mixture of tea catechins for **GT**-Fe_3O_4.

Recently, the synthesis of highly crystalline and monodispersed iron oxide NPs have been performed in nonaqueous media by the high-temperature decomposition of metal−organic compounds.[22−24] As the direct products are insoluble in aqueous media due to the hydrocarbon periphery of surfactants used, further tedious ligand−exchange procedures are required to produce aqueous suspensions, for instance, by surface immobilization of amphiphilic polymers.[25−28] Therefore, a facile, fast, and one step synthesis and *in situ* coating of iron oxide NPs that would make them water-soluble and biocompatible remains a persistent challenge for the preparative nanotechnology. We have recently reported on an easy synthetic pathway to prepare water-stable and easily dispersible SPIONs as MRI contrast agent by using vitamin C (ascorbic acid) as the reducing agent, whereby the *in situ* formed oxidation product dehydroascorbic acid acted as the stabilizer.[29] This chemically benign synthetic strategy inspired us to investigate the potential of other natural nutrients acting as efficient reducing and stabilizing agents for the green and scalable synthesis of high quality SPIONs for biomedical applications.[30]

Green tea serves as a popular and healthy beverage because of its well-known beneficial effects such as antioxidative, anticancer, anti-inflammatory and antithrombogenic activities, attributed to its polyphenolic contents (flavanol monomers), the so-called tea catechins (**TCs**) mainly consisting of epicatechin (**EC**), epicatechin gallate (**ECG**), epigallocatechin (**EGC**), and epigallocatechin gallate (**EGCG**), among which **EGCG** has the largest percentage (50−80%).[31,32] **TCs** are water-soluble and superior antioxidant agents because of the presence of catechol and pyrogallol groups that can readily react with oxidative species. Consequently, extensive efforts have been made to decipher the possible mechanisms of the cancer preventive effects of green tea polyphenols that include inhibition of free radical formation, lipid peroxidation, and the inhibition of DNA−carcinogen binding. In addition, auto-oxidation of green tea polyphenols generates H_2O_2, which has been found to induce apoptosis as well indicating that further efforts are necessary to explore the potential of **GT** polyphenols as chemopreventive or therapeutic agents. The reducing behavior of green tea polyphenols has been used to prepare a number of metal nanoparticles (e.g., Fe, Ag, Au, Pd) from corresponding ions and graphene colloids (obtained by reducing graphene oxide) stabilized by the green tea solution and its extracts;[33−39] however, the capping potential of the oxidized byproducts that can impart greater stability and water-dispersibility to the nanoparticles has not been investigated to the best of our knowledge. In addition, so far there is no report on the synthesis and functionalization of Fe_3O_4 NPs using green tea extracts. The green tea catechins offer a 2-fold advantage as reducing agent for metal cations: first, the electron-donating properties that would eventually cause oxidative stress in the cells can be buffered by Fe^{3+} centers that can accept the electrons and reduce to Fe^{2+} required to form the magnetite phase (Fe_3O_4); second, the fully or partially oxidized polyphenols form quinones or semiquinones that can chelate the surface of the iron oxide nanoparticles making them stable and water-dispersible. In this study, water-dispersible ultrafine SPIONs were obtained by the chemical reduction of $Fe(OH)_3$ colloids using green tea polyphenols as the reducing agents under mild hydrothermal conditions, whereby the reducing ability of catechins depend on the number of phenolic units. In vivo tumor accumulation and clearance of the particles investigated by dynamic MRI measurements of tumor regions in cancer-xenograft bearing mice. The results showed significant uptake of magnetite nanoparticles and no markedly adverse effect on the cell viability were observed making these particles in conjunction with their high colloidal stability and good T_2-values a promising candidate for various MR imaging purposes.

RESULTS AND DISCUSSION

In a typical synthesis of Fe_3O_4 quantum dots, Fe^{3+} was stoichiometrically reduced to Fe^{2+} by adding appropriate amount of **EGCG** and **EC** to obtain a $Fe(OH)_3/Fe(OH)_2$ colloid in 2:1 ratio (Scheme 1). The single-electron transfer reactions of individual catechins enabled the formation of single-phase Fe_3O_4 nanoparticles without facing the limitations, such as coexistence of various Fe:O compounds (FeO, Fe_2O_3, Fe_3O_4), often encountered in traditional coprecipitation methods.[2,11]

DOI: 10.1021/am508404t
ACS Appl. Mater. Interfaces 2015, 7, 6530−6540

Scheme 2. Basic Scaffold of the Polyphenol Structure Is Shown in Part A and the Functional Groups Present in the Epicatechin (EC) and Epigallocatechin-3-gallate (EGCG) are Shown in Parts B and C, Respectively[a]

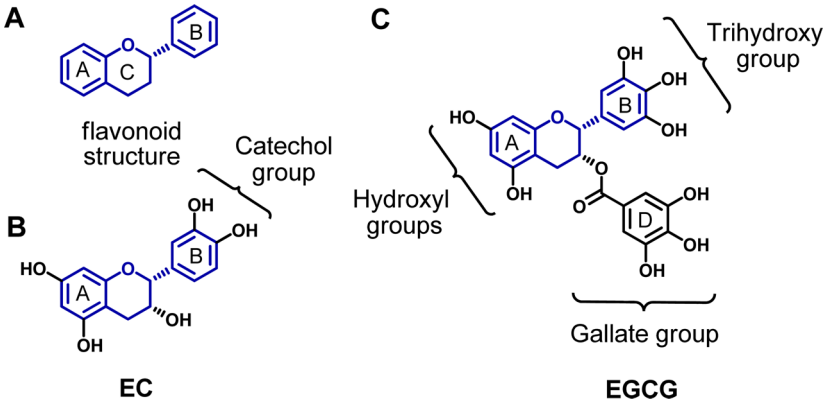

[a]The higher reduction potential of **EGCG** is caused by the additional ring D.

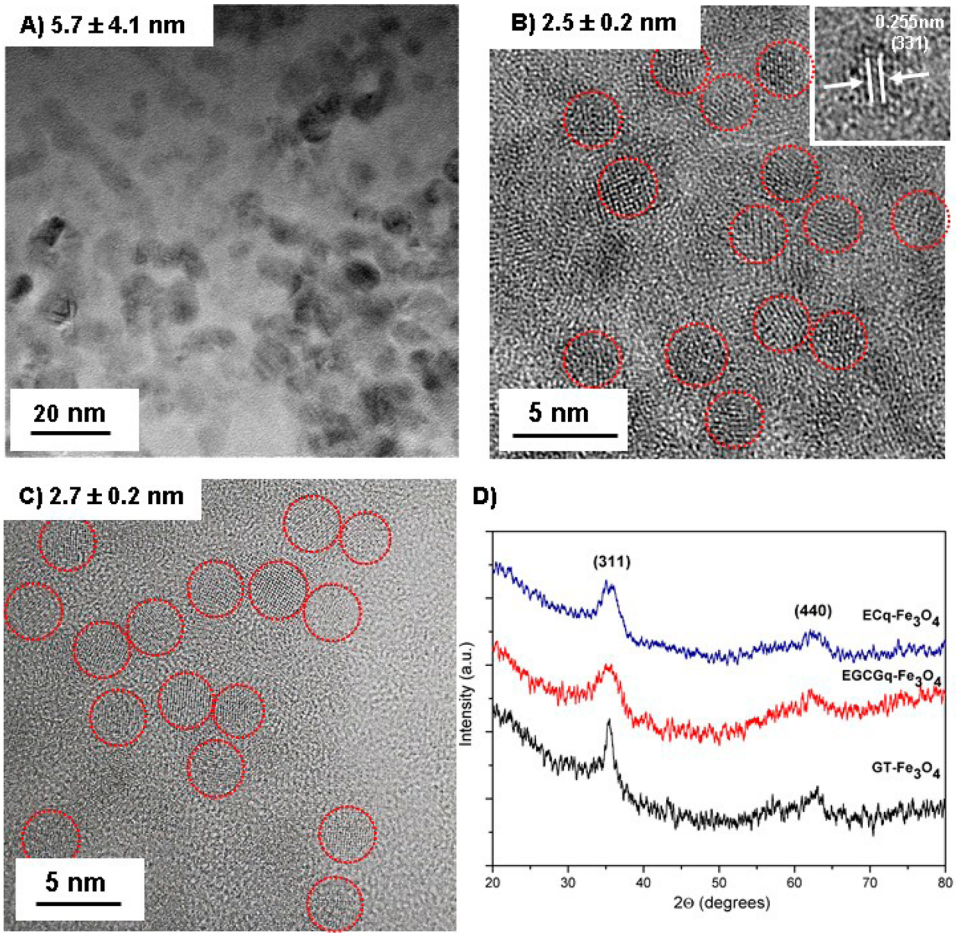

Figure 1. HR-TEM analysis of (A) **GT-Fe_3O_4**, (B) **EGCGq-Fe_3O_4**, and (C) **ECq-Fe_3O_4**. Figure B and C display the high crystallinity and regular dispersion of the particles. The XRD of **GT-Fe_3O_4**, **EGCGq-Fe_3O_4**, and **ECq-Fe_3O_4** is shown in D, confirmed the formation of cubic Fe_3O_4 phase.

During the redox process, the catechins **EGCG** and **EC** acted as the reducing agent (Scheme 2) by oxidizing the aromatic rings in their pyrogallol and gallic acid units (**EGCG**) and pyrocatechol units (**EC**).[35,39−41] In addition, their oxidation products (corresponding quinone forms, abbreviated as **EGCGq** and **ECq**)[35,39] also acted as stabilizers via the strong capping effect through the chemical interaction of the carbonyl groups or phenolic hydroxyls with FeO_x particles (Scheme 1).[29,42−45] The strong capping effect of both oxidized and free catechins provided good biocompatibility and high colloidal stability to magnetic nanoparticles in several media (vide infra).

The formation of the cubic phase of Fe_3O_4 NPs was confirmed by the XRD data (JCPDS No.89−0688) (Figure 1D) that was used to determine the average crystallite size (5.9 nm) in the samples by Debye−Scherer formula.[46] The peak broadening and uneven peak profiles were indicative of poor crystallinity and dispersion in crystallite size. The TEM image (Figure 1A) of the green tea stabilized magnetite NPs (**GT-**

DOI: 10.1021/am508404t
ACS Appl. Mater. Interfaces 2015, 7, 6530−6540

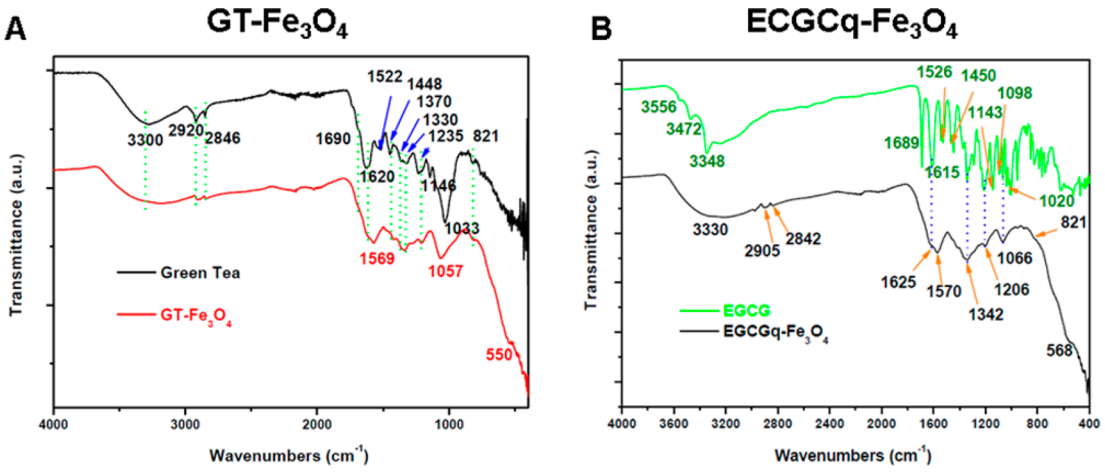

Figure 2. FT-IR analysis of (A) GT- and (B) EGCGq-Fe_3O_4 nanoparticles.

Fe_3O_4) also confirmed the inhomogeneity in the particle size distribution, possibly resulting from the differential reaction (reduction) kinetics of various catechins present in the green tea extract. Although the pK_a values of most phenols lies in the region 9−10, the protons can be displaced at much lower values (5−8) in the presence of suitable redox active cations (e.g., Fe(III) ← → Fe(II) shuttle). Therefore, metal chelation by phenolic groups can occur at physiological pH values, whereby polydentate ligands (several hydroxyl groups) are more powerful scavengers than monodentate phenols. As a result, the redox state of iron can be switched by manipulation of pH.

The organic surface modification of the **GT-Fe_3O_4** NPs was analyzed by differential peak analyses of the TGA and FTIR data of green tea and **GT-Fe_3O_4** samples (Figure 2A and Supporting Information Figure S2C). The amount of organic compounds present on the magnetite surface was found to be 36.1 wt % indicating strong absorption of green tea polyphenols on nanoparticle surface. This observation was confirmed by FTIR data that revealed phenolic hydroxyls and hydroxyls stretches of water molecules as a broad absorption band centered at 3300 cm^{-1}; the peaks at 2920 and 2846 cm^{-1} were due to CH_2 and CH groups, whereas signals at 1620 and 1448 cm^{-1} are characteristics of C═C stretching frequencies emerging from the aromatic rings of **TCs**. The bands at 1370 cm^{-1}, 1330 and 1146 cm^{-1} corresponded to the aromatic C−OH stretching mode; and the peak at 821 cm^{-1} was attributed to the C−O−C group present in the **TCs** structures.

The **GT-Fe_3O_4** NPs were redispersible in water, PBS and cell culture medium, presumably due to the capping effect from the active components of green tea (**TCs**). This was also reflected in the highly negative zeta potential (ζ = −35.8 mV) of the **GT-Fe_3O_4** NPs in aqueous solutions. Nevertheless, the DLS measurements in aqueous suspensions showed polydisperse behavior with an average size of 119 nm possibly due to a nonuniform size distribution and/or nanoparticle aggregation in solution (Supporting Information Figure S3A).

Although the concept of using green tea as an efficient reducing agent and source of *in situ* surface functionalization of water-soluble magnetite nanoparticles was successfully demonstrated, the control over the reaction kinetics and particle size-distribution was marginal. Therefore, in further experiments the green tea extracts of pure catechins **EGCG** and **EC** were used to control the reduction ability of the precursor solution and moreover to achieve a stronger stabilizing effect of the formed magnetite NPs. The direct reduction of Fe(III) to Fe(II) became immediately visible during the reaction as the red-brownish $Fe(OH)_3$ colloidal suspension immediately turned dark upon addition of the **EGCG** or **EC** solutions (Supporting Information Figure S6). The XRD patterns (Figure 1D and Supporting Information Figure S1) of the samples, synthesized using **EGCG** at different temperatures, were in good agreement with the ones prepared by **GT** exhibiting the presence of cubic spinel phase of Fe_3O_4 (JCPDS No.89-0688) as found in the case of iron oxide nanoparticles formed by reduction performed with **GT** extract. Nevertheless the peak profiles in the diffractograms of **EGCGq-Fe_3O_4** and **ECq-Fe_3O_4** samples exhibited higher crystallinity, although the peak broadness were indicative of smaller crystallite sizes. The crystallite sizes calculated from X-ray diffraction data revealed average particle sizes of 2.1, 2.2, and 2.4 nm for the **EGCGq** samples prepared at 160, 180, and 200 °C, respectively (Supporting Information Figure S1B). The very similar core-sizes suggested that the growth of Fe_3O_4 nanostructure has been inhibited even when the external thermal energy supply was increased. This could be attributed to the strong capping effect of **EGCGq** and **ECq** molecules on the NPs surface. Negatively charged ligands (upon deprotonation) tend to stabilize Fe(III) centers as electrostatic repulsion will favor removal of an electron from Fe(II). However, neutral ligands such as semiquinones or quinones, formed during the redox reactions, will stabilize the divalent state possibly due to the greater crystal field stabilization energy of a d^6 (Fe(II)) system compared to that of d^5 state (Fe(III)). These effects are active in the chelation of the surface sites of Fe_3O_4 nanostructures that consist of **−Fe(II)−O−Fe(III)−O−** units.

The HR-TEM image (Figure 2B) of the **EGCGq-Fe_3O_4** NPs prepared at 200 °C showed spherical crystallites with a narrow size distribution (2.5 ± 0.2 nm) that was similar to the size calculated based on the XRD data. The presence of magnetite phase was further confirmed by the interplanar distance of 0.255 nm corresponding to the lattice spacing of the (311) planes of Fe_3O_4. A similar size distribution and morphology was also observed in the HR-TEM of **ECq-Fe_3O_4** (Figure 2C).

Scheme 1 illustrates a possible formation mechanism of the **EGCGq** capped Fe_3O_4 NPs from the redox chemistry involved between **EGCG** and $Fe(OH)_3$. The formation mechanism of **GT-Fe_3O_4** and **ECq-Fe_3O_4** is apparently similar except that a mixture of tea catechins or **EC** was used as reduction agent

DOI: 10.1021/am508404t
ACS Appl. Mater. Interfaces 2015, 7, 6530−6540

instead of **EGCG**. As the antioxidant property of **EGCG** is given by its pyrogallol and gallic acid units, the presence of an oxidative species (here $Fe(OH)_3$) will oxidize these functional groups into corresponding quinones (Scheme 1A). The oxidation of **EGCG** to form **EGCGq** can be monitored by the FTIR spectra (Figure 2B) revealing the disappearance of the absorption bands due to alkene (C═C) and phenolic hydroxyl groups in the aromatic rings, as well by appearance of a new band corresponding to carbonyl groups (C═O).[35,4] Upon addition of the appropriate amounts of catechins, one-third of the $Fe(OH)_3$ was reduced to $Fe(OH)_2$ by **EGCG**, thereby generating the oxidized quinone form **EGCGq** (Scheme 1b). This was followed by the mild hydrothermal treatment wherein the **EGCGq** could attach onto and stabilize the formed Fe_3O_4 NPs. In the FTIR spectrum of **EGCGq-Fe_3O_4** NPs (Figure 2B) the bands at 1689 and 1526 cm^{-1} corresponding to the C═C vibration located in the trihydroxy-aromatic rings disappeared as well as the bands at 1143, 1098 and 1020 cm^{-1} due to the phenolic hydroxyl groups present in **EGCG** (Figure 2B). This suggested that the **EGCG** was oxidized and absorbed on the Fe_3O_4 NPs. However, the absorption band around 1720 cm^{-1} belonging to the carbonyl groups C═O of **EGCGq** molecules was also not observed in the spectrum. This phenomenon is known for the dehydroascorbic acid capped Fe_3O_4 NPs, where the diminished C═O stretch was attributed to the strong bonding interaction between the carbonyl groups and the Fe center on the surface of the NPs.[29,47−50] A new absorption band centered around 1570 cm^{-1} could possibly be due to this interaction. The remaining phenolic hydroxyl groups appeared as a broad peak centered at 3300 cm^{-1} indicating the hydrogen bonding among the **EGCGq** molecules; the absorption bands at 2905 and 2842 cm^{-1} originate from $-CH_2$ and $-CH$ groups; the remained aromatic hydroxyl groups also reflected two broadened bands centered at 1342 and 1066 cm^{-1} and a slightly shifted band at 1206 cm^{-1}suggesting an interaction of the hydroxyl groups with the surface of the NPs and furthermore, the existence of hydrogen bonding. At last the absorption shoulder at 821 cm^{-1} could be assigned to C−O−C vibrations and the band at 553 cm^{-1} to the Fe−O lattice vibrations. In conclusion, the bonding through the carbonyl and the phenolic hydroxyl groups of the **EGCGq** molecules toward the Fe_3O_4 NPs was confirmed by FTIR data. Similar observations were made for the FT-IR analysis of **ECq-Fe_3O_4** nanoparticles (Supporting Information Figure S2A).

After the purification process, the **EGCGq-Fe_3O_4** NPs and **ECq** showed an excellent redispersibility in water by manual shaking, as well as in PBS and cell culture medium (Figure 3).

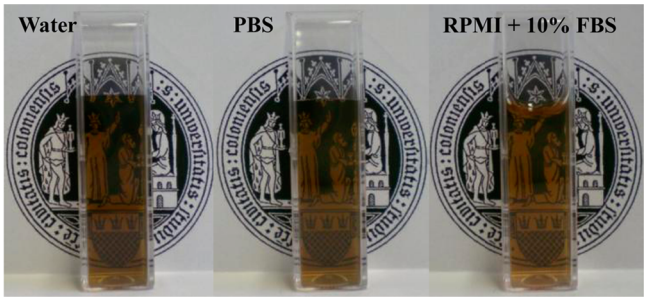

Figure 3. Dispersions of EGCGq-Fe_3O_4 NPs in water, PBS, and RPMI (10% FBS).

The presence of organic ligands responsible for dispersibility in protic reagents was verified by the thermal gravimetric analysis of the washed specimens. The organic fraction of **EGCGq-Fe_3O_4** and **ECq-Fe_3O_4** NP was estimated to be 31.2% and 30.5%, respectively (Supporting Information Figure S2B and S2D) that confirmed the tight capping of **ECq** and **EGCGq** on the NP surface.

The obtained aqueous suspension of **EGCGq-Fe_3O_4** and **ECq-Fe_3O_4** showed an excellent shelf life in concentrated form in the absence of any further surface modification or additives. Additionally, no noticeable precipitation was observed for both NPs. The average hydrodynamic sizes of NPs monitored by Dynamic Light Scattering (DLS) studies were found to be 64 nm for **EGCGq-Fe_3O_4** and 56 nm for **ECq-Fe_3O_4**, respectively (Supporting Information Figure S3B and C) based on the scattering intensity (d_{DLS}) measured in backscattering geometry. The larger hydrodynamic radii suggested the appearance of agglomerated particles in the suspension, probably due to the interparticle interaction triggered by the surface-attached **EGCGq** or **ECq** molecules via their outer shell of −OH groups. Nevertheless, the polydispersity index (PDI) of 0.20 and 0.19, respectively, indicated relatively monodisperse distribution. The **EGCGq-Fe_3O_4** particles showed a high negative ζ-potential of −38.3 mV at pH 5.7. Similar values were observed at pH 6, where the particles showed a ζ-potential about −29 mV. Therefore, we infer that **EGCGq-Fe_3O_4** and **ECq-Fe_3O_4** suspensions exhibit unusual stability and favorable colloidal properties in suspension useful for biological applications.

The temperature-dependent magnetic behavior of **GT-Fe_3O_4** NPs, **EGCGq-Fe_3O_4** and **ECq-Fe_3O_4** NPs were determined by zero field cooling (ZFC) and field cooling (FC) measurements (Figure 4A and Supporting Information Figure S5). For the ZFC measurements, first the samples were cooled down from 300 to 2 K without any external magnetic field, and then the magnetizations were recorded while heating up the samples at an applied field of 500 Oe. The magnetization value increased with the increasing of temperature and reached the maximum defined as the blocking temperature (T_B), which was 59 K, 15 and 16 K for **GT-Fe_3O_4** NPs, **EGCGq-Fe_3O_4** and **ECq-Fe_3O_4** NPs, respectively. The ZFC curves dropped down with further increasing the measuring temperature because of the thermal energy overcoming the interparticle magnetic couplings. The magnetization value of **GT-Fe_3O_4** NPs, as expected, is higher than that of **EGCGq-Fe_3O_4** NPs and **ECq-Fe_3O_4**, as the particles in the latter two samples magnetically perform more decoupled. However, the ZFC curve of **GT-Fe_3O_4** NPs separated from its FC curve at a point (irreversibility temperature,[51] T_I = 59 K) higher than the T_B, indicating that some larger particles exist as already discussed above; moreover, the broadening of the ZFC peak implies a range of magnetic interaction strengths between the iron oxide nanoparticles.[52,53] In contrast, the **EGCGq-Fe_3O_4** and **ECq-Fe_3O_4** NPs exhibited a much sharper ZFC peak that left its FC curve at T_B, which could be attributed to the narrow particle size distribution of the **EGCGq-Fe_3O_4** and **ECq-Fe_3O_4** NPs. The blocking temperatures of **EGCGq-Fe_3O_4** NPs synthesized at higher temperature were slightly increased (Supporting Information Figure S4B) since the crystallite sizes were enhanced a bit, which is consistent with the Néel's theory.[54]

In general, the magnetization behavior for all three samples was observed to be superparamagnetic with M_s value of 16.7, 14.8, and 20.2 emu/g for **TG-Fe_3O_4**, **EGCGq-Fe_3O_4** and **ECq-**

DOI: 10.1021/am508404t
ACS Appl. Mater. Interfaces 2015, 7, 6530−6540

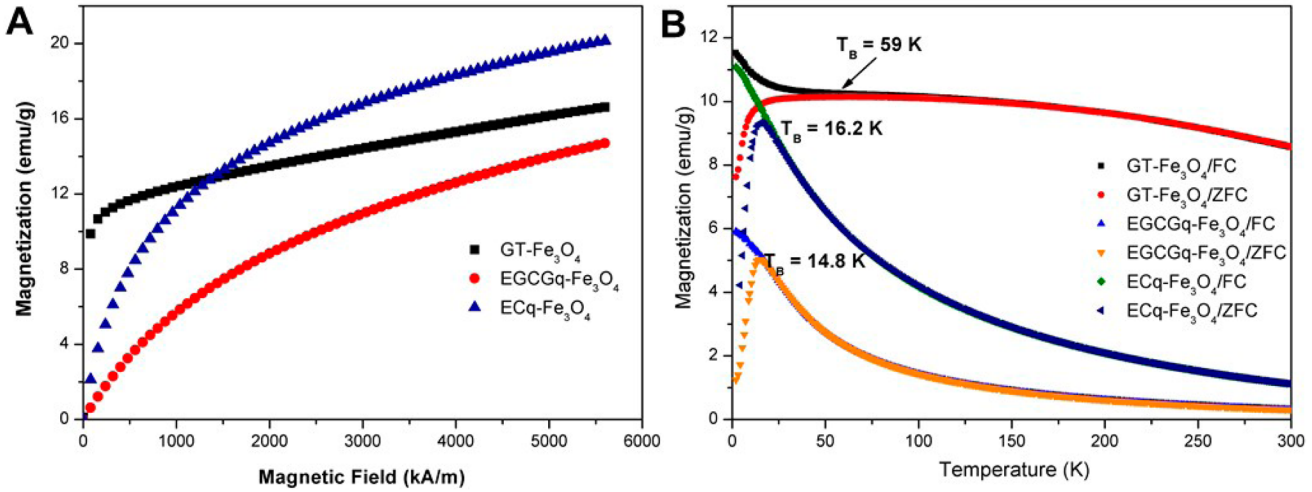

Figure 4. (A) Saturation magnetization (M_s) measurements of **GT-Fe_3O_4**-, **ECq**-, and **EGCGq-Fe_3O_4** NPs carried out at 300 K. (B) ZFC/FC measurements of **GT-Fe_3O_4**, **EGCGq**-, and **ECq-Fe_3O_4** NPs; measurements were carried out at 500 Oe, in the temperature of 2−300 K. The measurement reveals the different T_B values of the as prepared NP.

Fe_3O_4, respectively (Figure 4B and Supporting Information Figure S5). The hysteresis loop (Supporting Information Figure S4A) of **EGCGq-Fe_3O_4** NPs (up to 70 kOe) recorded at 2 K, below T_B, displays a hysteretic behavior with a low remanence of 5.8 emu/g and a saturation magnetization (M_s) value of 29.8 emu/g. The magnetization behavior (Supporting Information Figure S4A), however turned to superparamagnetic when the measurement was recorded at 300 K, and it reached a smaller M_s value of 14.8 emu/g because of the the stronger thermal influence (Figure 4B).

Relaxivity Measurements. To evaluate the imaging properties of the particles, phantom experiments with dilution series were performed using a clinical 3 T MRI scanner. A clearly observable negative contrast was detected in T_2-weighted images from concentrations of 0.1 mM **GT-Fe_3O_4**, 0.3 mM **ECq-Fe_3O_4**, and **EGCGq-Fe_3O_4**, respectively. As expected, signal intensity in T_1-weighted images only decreased slightly in higher concentrations of 1.0 and 1.3 mM (Figure 5A). Relaxivity values were determined from a dilution series in 5% glucose at RT: **GT-Fe_3O_4** r_1 = 0.368 s^{-1} mM^{-1}, r_2 = 77.14 s^{-1} mM^{-1} (r_2/r_1 = 209.6); **ECq-Fe_3O_4** r_1 = 0.688 s^{-1} mM^{-1}, r_2 = 36.31 s^{-1} mM^{-1} (r_2/r_1 = 52.77); **EGCGq-Fe_3O_4** r_1 = 0.380 s^{-1} mM^{-1}, r_2 = 36.18 s^{-1} mM^{-1} (r_2/r_1 = 95.21) (Figure 5B).

r_2 values were for all of the particles in the range of clinically approved agents (Sinerem = 60 s^{-1} mM^{-1}, Ferridex = 98 s^{-1} mM^{-1}).[55] The high r_2/r_1 ratios, especially for **GT-Fe_3O_4**, illustrate their superior potential for T_2-weighting at reasonable concentrations.

Magnetic relaxivity of iron oxide nanoparticles is mainly determined by iron core size, composition, crystalline phase, as well as property and thickness of the surface coating. The higher r_2 value for **GT-Fe_3O_4** compared to **EGCGq-Fe_3O_4** and **ECq-Fe_3O_4**, can therefore be explained on the one hand by the larger iron core size (5.1 versus 2.2 (**EGCGq-Fe_3O_4**) and 2.7 nm (**ECq-Fe_3O_4**)) and on the other hand by the larger hydrodynamic size of the particles (119 versus 64 (**EGCGq-Fe_3O_4**) and 56 nm (**ECq-Fe_3O_4**)).

Cellular Uptake. The cellular uptake of **GT**-, **ECq**-, and **EGCGq**-coated iron oxide nanoparticles in CT26 and J774A.1 was investigated by MRI (at 3T) (Figure 6A). The cells were labeled with the particles at concentrations ranging from 0.03 to 1.3 mM for 3 h. After they were extensively washed, 2×10^6 labeled cells were suspended in 300 μL of 10% gelatin and measured in T_2-weighted MRI. CT26 cells showed a strong negative contrast after 3 h of incubation with 0.1 mM **GT-Fe_3O_4**, whereas concentrations of 1 mM and 0.6 mM were needed to observe particle uptake of **ECq**- and **EGCGq-Fe_3O_4** in the cells, respectively. Since there is no known receptor for catechins, receptor-mediated uptake of the particles seems unlikely. Instead internalization might likely be mediated by the receptor-independent caveolin or clathrin routes. The stronger contrast enhancement of **GT-Fe_3O_4** labeled cells can be explained by the higher r_2 value of these particles. However, it was demonstrated that r_2 is approximately twice as high as for the other particles, whereas the cell uptake appears by a factor 6 to 10 more efficient for **GT-Fe_3O_4** compared to **ECq**- and **EGCGq-Fe_3O_4**. This effect could be attributed to the size differences between the particles or to the fact that the **GT** coating consists of an extract of several molecules instead of just one functional molecule, what might promote multivalent interactions with the cell surface. In J774A.1, all particles showed a similar uptake from concentrations of 0.1 mM for **ECq**- and **EGCGq-Fe_3O_4**, and 0.03 for **GT-Fe_3O_4**.

Cytotoxicity. Nanoparticle-induced cytotoxicity was assessed by MTT assay (Figure 6B). Only a slight reduction in metabolic activity was observed in CT26 after 3 h exposure to 1.3 mM of iron oxide nanoparticles. In J774A.1 a decrease of metabolic activity could be observed also in lower concentrations of 0.3 mM, likely due to the high uptake and consequently the high intracellular iron load. In the concentrations ranges, which already promoted a significant uptake of the particles (0.3−1.0 mM for CT26, 0.1 mM for J744A.1) the cell metabolism was for both cell lines not significantly affected by the particle uptake. Even **GT-Fe_3O_4** which showed a higher cell uptake in lower concentrations compared to the other nanoparticles, showed no increased cytotoxicity.

In Vivo Studies. *In vivo* tumor accumulation and clearance of the particles were assessed by dynamic MR measurements of caval vein, liver, and tumor regions after injection of 100 μL (600 mM) of the iron oxide nanoparticles. Tumor accumulation could be observed for all of the particles directly after

DOI: 10.1021/am508404t
ACS Appl. Mater. Interfaces 2015, 7, 6530−6540

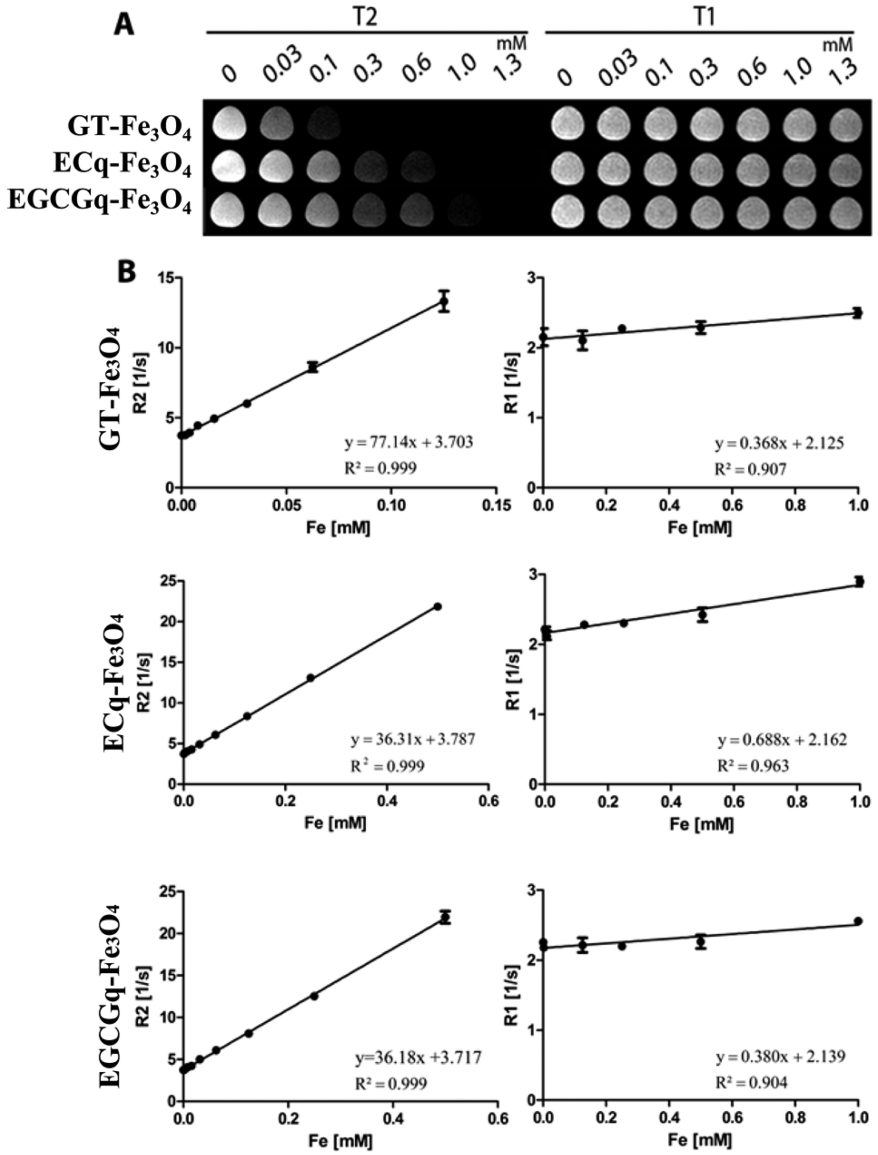

Figure 5. Relaxivity measured at a clinical 3T MRI scanner. (A) T_1- and T_2-weighted images of **GT**-, **ECq**- and **EGCGq**-coated iron oxide nanoparticles. The plots for the relaxivity (r_1 and r_2) determination are shown in panel B. All particles showed high r_2/r_1 ratios indicating their potential application as *T2* contrast agent.

injection, indicated by a decrease of signal intensities (Figure 7 A, C, E).

The blood half-life times were between 1−1.5 min for Resovist and **ECq-Fe_3O_4**, whereas for **GT**- and **EGCGq-Fe_3O_4** they were ten times shorter (around 0.1 min) (Figure 7 B, E). Since the size-difference in **EC** and **EGCG**-coated particles is marginal, the faster clearance is possibly due to the different surface chemistries as manifested in the differential Zeta potential values. All particles showed a strong uptake in the liver indicating rapid hepatic clearance after injection (Figure 6 C, E).

CONCLUSIONS

Superparamagnetic iron oxide nanoparticles coated with green tea quinones were successfully synthesized by a facile redox chemistry involving oxidative iron hydroxide colloids and electron-donating green tea poly phenols. Green tea catechins proved to be efficient reducing agents with synergistic interactions between the resulting oxidative products (semi-quniones and quinones) that *in situ* capped the as-formed Fe_3O_4 nanoparticles imparting them high stability at physiological pH and long shelf life in water-based dispersions. **GT**-capped Fe_3O_4 nanoparticles had a higher r_1/r_2 value than **EGCGq-Fe_3O_4** (209.6 versus 95.21) and were preferentially taken up by CT26 cells. As there is no particular receptor known for catechins, this might be caused by the variety of surface ligands originating from the **GT** compared to its **EGCG** extract. Both particles did not markedly affect viability of CT26 and J774A.1 cells, which make these particles, coupled with their high colloidal stability, their biocompatible surface capping and good T_2-values a promising candidate for various MR imaging purposes.

METHODS

Materials. The green tea named Longjing was purchased from a local market in China; (−)-Epigallocatechin gallate (90%) were ordered from Sigma-Aldrich, Germany; $FeCl_3{\cdot}6H_2O$ (99%+), and

DOI: 10.1021/am508404t
ACS Appl. Mater. Interfaces 2015, 7, 6530−6540

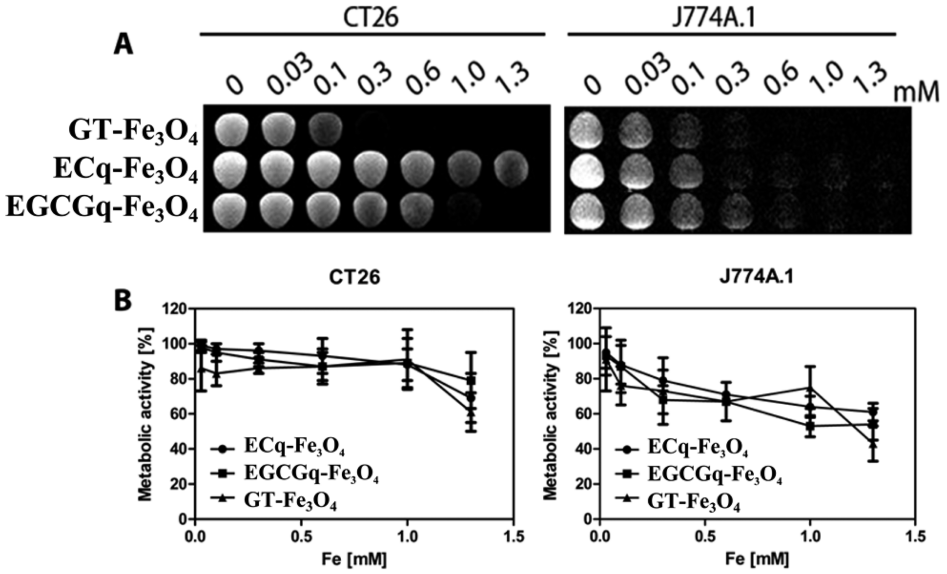

Figure 6. Nanoparticle uptake analyzed by means of MRI. (A) T_2-weighted images of CT26 and J774A.1 cells in gelatin (2×10^6 cells/0.3 mL) incubated with increasing concentrations of **GT-**, **ECq-**, and **EGCGq**-coated iron oxide nanoparticles for 3 h. The increasing negative contrast in T_2-weighted images clearly demonstrate the particle uptake. (B) Metabolic activity of cells upon exposure to increasing concentrations of iron oxide nanoparticles, as assessed by MTT assay. Cells were incubated with nanoparticles or remained untreated (control) for 3 h. The lines represent mean ± standard deviation (n = 3).

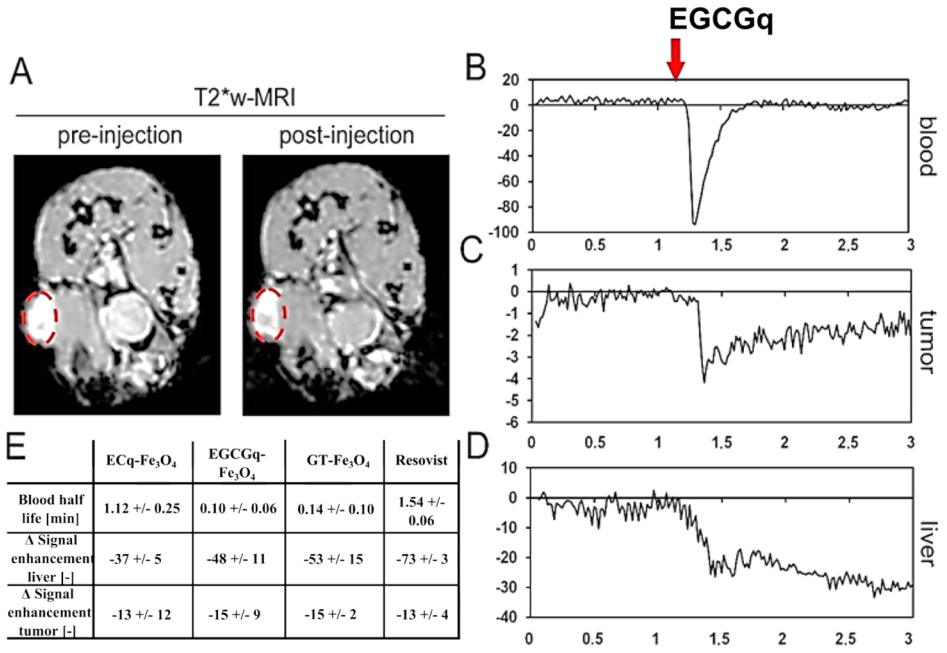

E	ECq-Fe_3O_4	EGCGq-Fe_3O_4	GT-Fe_3O_4	Resovist
Blood half life [min]	1.12 +/- 0.25	0.10 +/- 0.06	0.14 +/- 0.10	1.54 +/- 0.06
Δ Signal enhancement liver [-]	-37 +/- 5	-48 +/- 11	-53 +/- 15	-73 +/- 3
Δ Signal enhancement tumor [-]	-13 +/- 12	-15 +/- 9	-15 +/- 2	-13 +/- 4

Figure 7. Dynamic contrast enhanced (DCE)-MR measurement in mice after intravenous administration of **EGCGq-**, **ECq-**, **GT-Fe_3O_4**, and Resovist (A) T_2* weighted images before and after injection. A slight darkening of the tumor region (marked in red) could be observed indicating nanoparticle accumulation. (B–D) Exemplary signal-time curves of regions covering vessel (vena cava) (B), tumor xenograft (C), and liver (D), demonstrating the decrease of signal intensity after **EGCGq-Fe_3O_4** injection (red arrow). (E) Blood half-life and differences in signal intensity in liver, vessel, and tumor regions before and after injection were calculated by nonlinear regression analysis of the signal-time curves. Strongest signal was detected in the liver indicating hepatic clearance of the particles upon injection.

Na_2CO_3 (99.5%) were ordered from Acros Organics, Germany. All the chemicals were used without any further purification.

Preparation of the GT-Fe_3O_4 NPs. For the tea solution, 1.0 g of ground green tea powder was added into 30 mL of DI water and refluxed at 80 °C for 30 min, and then the mixture was filtered for 2 times. For the $Fe(OH)_3$ colloid solution, 1.0 mmol $FeCl_3 \cdot 6H_2O$ was dissolved in 20 mL of DI water under stirring for 10 min, and then 5 mL of 0.3 M Na_2CO_3 aqueous solution was added gradually and the obtained solution was stirred for 30 min. Subsequently, 10 mL of the green tea solution was added into the prepared $Fe(OH)_3$ colloid solution gradually. During the process, the color of the colloid solution changed from red-brown to black immediately when the green tea solution was dropped in, which indicated that the redox reaction occurred. The mixture was further stirred for another 10 min, and then transferred into a steel-lined Teflon autoclave with a volume capability of 40 mL, which was kept at 200 °C for 3 h.

Preparation of the EGCGq-Fe_3O_4 and ECq-Fe_3O_4 NPs. Instead of the tea solution, 10 mL of **EGCG** water solution in a molar ratio to

DOI: 10.1021/am508404t
ACS Appl. Mater. Interfaces 2015, 7, 6530–6540

Fe^{3+} of 1:12 (for **EC** the ratio was 1:6) was added gradually. The mixture was further stirred for 10 min, and then transferred into a steel-lined Teflon autoclave with a volume capability of 40 mL. The autoclave was kept at 200 °C, for 3 h. For comparison, the reactions were also carried out at 160 and 180 °C for 3 h, respectively. After the synthesis, the particles were washed with water for 3 times and finally were collected by centrifugation (11,000 rpm, 1 h for each time). The obtained precipitate can be easily redispersed in water, PBS buffer and cell cultures medium by ultrasonication (180 s, SONOREX SUPER RK 510 H, 35 kHz, 640 W).

Characterization of GT-Fe_3O_4, EGCGq-Fe_3O_4, and ECq-Fe_3O_4 NPs. The basic physic-chemical characterizations of the **GT-Fe_3O_4** and **EGCG-Fe_3O_4** NPs have been done by TEM, XRD, FTIR, and TGA. TEM images were obtained with a Philips CM300 microscope. The phase composition of the as-prepared sample was characterized with a STOE-STADI MP X-ray powder diffraction meter operating in a transmission mode using CuKα (1.5406 Å) radiation. FT-IR spectra were recorded on a PerkinElmer FTIR spectrometer. Thermogravimetric analysis (TGA) was performed with a TGA Q50 (TA Instruments) instrument in a flowing air atmosphere employing a heating rate of 10 °C/min.

Magnetization and Zero-Field-Cooling (ZFC) and Field-Cooling (FC). The saturation magnetization (Ms) and ZFC/FC for the prepared magnetite NPs were investigated on a SQUID magnetometer (Quantum Design, MPMS XL-7): for the Ms values, the dried samples were measured in the magnetic field range of 0−70000 Oe at 2 and 300 K, respectively; for the ZFC/FC magnetization, the measurements were carried out under 500 Oe in the temperature of 2−300 K.

Determination of Iron Content. Total Fe was determined by inductively coupled plasma atomic emission spectroscopy (ICP-AES) on a Varian Liberty 220ICP. The suspension was prepared by combining a 0.2 mL aliquot of the sample with 0.5 mL of 8.8 N analytical grade HCl and 1 mL of deionized water. The mixture was heated until only ∼1 drop of liquid remained, at which time 10 mL deionized water was added. The solution was heated to boiling and then immediately removed from the heat and allowed to cool to room temperature. The volume was adjusted to 50 mL for spectrometric analysis.

Dynamic Light Scattering. The DLS experiments were performed at 25 °C on a NanoZS (Malvern Instruments, Malvern UK) which uses a detection angle of 173°, and a 3 mW He−Ne laser operating at a wavelength of 633 nm. The Z-Average diameter, d_{hyd}, and the polydispersity index (PDI) values were obtained from analysis of the correlation functions using Cumulants Analysis. Zeta potential measurements were performed at 25 °C on the NanoZS, using the M3-PALS technology. In all cases the DLS and Zeta potential measurements were recorded on diluting samples in the concentration range of 1−5 mM.

3T MR-Imaging and Relaxometry. MR-imaging and MR-relaxometry at 3T (127.7 MHz) was performed in a clinical whole-body MR scanner (PHILIPS Achieva, The Netherlands) using a ring coil (SENSE-flex-M, PHILIPS, The Netherlands) at room temperature. Nanoparticle water suspensions were diluted in 5% glucose solutions at Fe concentrations ranging from 0.0019 to 1.0 mM. For MR measurements 0.3 mL/well of the diluted solution was filled in custom-made phantoms (Greiner 96 well Flat Transparent Polystyrol microplate, Germany). Transverse relaxation times (T_2) were measured in 3D scan mode using a multislice, multi shot spin echo sequences with 90° excitation pulses followed by a train of equally spaced 180° refocusing pulses [TR = 1500 ms, TE = 11.8 ms, number of echoes = 20, FOV = 180 × 229, matrix = 8815, slice thickness 3 mm]. Longitudinal relaxation times (T_1) were determined using a 2D multishot spin echo sequences with a nonslice selective inversion pulse (180°) followed by multiple low flip-angle slice selective excitation pulses (10°) to repeatedly sample the longitudinal magnetization during its recovery [TR = 6.8 ms, TE = 3.3 ms, number of echoes =1, FOV = 170 × 148.75 mm, matrix = 152 × 130, slice thickness = 5 mm]. Relaxivities r_1 and r_2 were determined by a linear fit of the inverse relaxation times as a function of the iron concentrations.

Furthermore, T_1-, T_2-, and T_2*-weighted images were acquired using the following sequences: T_1-weighted turbo spin echo (TSE) sequence, [TR = 500 ms, TE = 20 ms, FOV = 150 mm, matrix =304 × 240, slice thickness = 5 mm], T_2-weighted TSE sequence [TR = 206m s, TE = 100 ms, FOV = 200 mm, matrix size = 1008, slice thickness = 2 mm]; T_2*-weighted TFE imaging sequence [TR = 14 ms, TE = 5 ms, FOV = 30 mm, matrix =144, slice thickness =2 mm].

Cell Culture. CT26 and J774A11 cells were cultured using DMEM (Gibco, Invitrogen, Germany) cell culture medium supplemented with 10% fetal calf serum (Invitrogen, Germany) and 1% Pen/strep (10 000 U/mL penicillin; 10 000 mg/mL streptomycin, Invitrogen, Germany). Cells were cultured in T75 cell culture flasks (Cell star, Greiner, Germany) and incubated at 37 °C, 5% CO_2 and 95% relative humidity.

Cell Uptake. The intracellular uptake of the iron oxide nanoparticle in CT26 and J774A.1 cells was investigated using MRI. The nanoparticles were diluted in cell culture media, to have final iron concentration of 0.03, 0.1, 0.3, 1.0, and 1.3 mmol Fe/mL. CT26 and J774A.1 cells were cultured in T75 cell culture flasks with DMEM cell medium (with 10% FCS, 1% Pen/Strep) at 37 °C, 5% CO_2, and 95% relative humidity until 70% confluency was reached. The supernatant medium was removed when 80% confluency was reached and cells were washed once with PBS buffer. Subsequently, cells were labeled with 11 mL of medium with nanoparticles and controls. Three samples per condition were analyzed. Cells were incubated for 3 h at 37 °C, 5% CO_2 and 95% relative humidity. After incubation, cells were washed once with PBS and subsequently trypsinized using 5 mL of trypsin/EDTA (0.25%/0.5%). Trypsinization was stopped by adding cell culture medium and the cell suspension was centrifuged at 1000 rpm (Multifuge, Thermo Scientific, Germany) for 5 min. The cell pellet was resuspended in 20 mL of PBS buffer and washed three times by performing the centrifugation as described above. The total cell numbers in the suspension were counted and after washing the cell pellet with PBS, it was dissolved in 10% gelatin to have 2×10^6 cells/0.3 mL as final cell concentration. MR-relaxometry of cells was performed at 3T using the MR-sequences described before.

MTT Cytotoxicity. Cell viability of CT26 and J774A.1 cells exposed to iron oxide nanoparticles was determined using Roche Cell Proliferation Kit I (MTT) (Roche, Switzerland), which is based on the reduction of the tetrazolium salt MTT by viable cells. CT26 and J774A.1 cells were seeded on 96 well plates with DMEM cell medium (with 10% FCS, 1% Pen/Strep) and cultivated at 37 °C, 5% CO_2, and 95% relative humidity until 70% confluency was reached. Afterward, the medium was exchanged by iron oxide solutions prepared with DMEM cell media in iron concentrations ranging from 0.03 to 1.3 mM. 300 μL of the solution with the desired concentrations were added to each well. Cells were incubated with the particle solutions for 3 h at 37 °C, 5% CO_2, and 95% relative humidity. After incubation, the wells were washed once with 150 μL of PBS. The MTT solution was prepared according to the protocol provided by the company. The MTT stock solution (5 mg/mL in PBS) was mixed with DMEM (1:10). 100 μL of the final mixture were then added to each of the wells and the plates were incubated at 37 °C for 4 h. Afterward the supernatants were removed and the wells were filled with 200 μL of DMSO solutions to solve the Formazan salt produced. The plate was kept at room temperature in a hood covered with an opaque material for 1 day. The supernatant were transferred to a new 96 well plate and the absorbances were measured with a Tecan reader at 570 nm with a reference wavelength of 690 nm. The values were plotted versus the corresponding concentrations.

In Vivo Study. All experiments were approved by the Governmental Review Committee on Animal Care. In total, 12 female CD1-nude mice (Charles River, strain code 086) were used for the evaluation of **EGCG**, **EC**, **GT**, and **Resovist**. The epidermoid carcinoma cell line A431was cultivated in Dulbecco's Modified Eagle Medium (DMEM; Gibco, Invitrogen GmbH) containing 10% FBS (Gibco) and 1% penicillin/streptomycin (Gibco). A total number of 4×10^6 A431 cells in 100 μL of culture medium was injected subcutaneously into the right flank of 6- to 8-week-old mice. Ten days after injection, the tumors had reached a size of approximately 4−5 mm in diameter and MR analysis was performed.

DOI: 10.1021/am508404t
ACS Appl. Mater. Interfaces 2015, 7, 6530−6540

DCE-MRI and Data Analysis. MRI was conducted at a clinical 3-T whole-body scanner (Achieva 3.0 T, Philips), using a small-animal solenoid receiver coil (Philips). For the MRI measurements, the animals were anesthetized with isofluorane (1.5%). For assessing tumor, liver and Vena cava, MR images were acquired using a transversal T_2*-weighted fast-field echo sequence (TR = 387 ms; TE = 10.2 ms; flip angle = 30°; matrix size = 144 × 144, scan mode = MS). DCE-MRI scans were conducted using a multi slice 2-dimensional (2D) T_{2w} saturation recovery gradient echo sequence (saturation recovery turbo fast low angle shot), TR = 71.25 ms, TE = 10.85 ms, flip angle = 30°, matrix = 112 × 112. In total, 300 sequential images were acquired per slice with a temporal resolution of 2.2 s, resulting in a total scan time of 11 min. After the acquisition of baseline images over approximately 1−1.5 min, 100 μL (6 mM) of the iron oxide nanoparticles were injected manually into the tail vein within 15 s.

The average signals of regions covering tumor, liver or vessel were computed using DynaLab Software and signal−time curves were plotted. Nonlinear regression analysis using GraphPad Prism software was applied to calculate the blood half-life and the differences in signal intensity before and after injection.

■ ASSOCIATED CONTENT

Ⓢ Supporting Information

Detailed FTIR, TGA, and DLS studies and visualization of the color change of the nanoparticle suspension during the synthetic process. This material is available free of charge via the Internet at http://pubs.acs.org.

■ AUTHOR INFORMATION

Corresponding Author

*E-mail: sanjay.mathur@uni-koeln.de. Fax: (+49)-221-470-4899.

Notes

The authors declare no competing financial interest.

■ ACKNOWLEDGMENTS

This work was funded by the University of Cologne and the EU Project "NANOMMUNE" (2009-12). The support through NRW/EU-Ziel 2-Programm (EFRE) 2007-2013: "Entwicklung und Bildgebung patientenoptimierter Implantate", the European Research Council (ERC Starting Grant 309495: NeoNaNo), Helmholtz-Society Portfolio Grant "Technologie und Medizin: Multimodale Bildgebung zur Aufklärung des In-vivo-Verhaltens von polymeren Biomaterialien", and ERS Boost Fund Program at RWTH Aachen University is gratefully acknowledged.

■ REFERENCES

(1) Ilyas, S.; Ilyas, M.; van Der Hoorn, R. A. L.; Mathur, S. Selective Conjugation of Proteins by Mining Active Proteomes through Click-Functionalized Magnetic Nanoparticles. *ACS Nano* **2013**, *7*, 9655−9663.

(2) Laurent, S.; Forge, D.; Port, M.; Roch, A.; Robic, C.; Vander Elst, L.; Muller, R. N. Magnetic Iron Oxide Nanoparticles: Synthesis, Stabilization, Vectorization, Physicochemical Characterizations, and Biological Applications. *Chem. Rev.* **2008**, *108*, 2064−2110.

(3) Xie, J. I. N.; Liu, G.; Eden, H. S.; Ai, H. U. A.; Chen, X. Surface-Engineered Magnetic Nanoparticle Platforms for Cancer Imaging and Therapy. *Acc. Chem. Res.* **2011**, *44*, 883−892.

(4) Xie, J.; Xu, C.; Kohler, N.; Hou, Y.; Sun, S. Controlled PEGylation of Monodisperse Fe_3O_4 Nanoparticles for Reduced Non-Specific Uptake by Macrophage Cells. *Adv. Mater.* **2007**, *19*, 3163−3166.

(5) Doane, T. L.; Burda, C. The Unique Role of Nanoparticles in Nanomedicine: Imaging, Drug Delivery and Therapy. *Chem. Soc. Rev.* **2012**, *41*, 2885−2911.

(6) Huh, Y.; Jun, Y.; Song, H.; Kim, S.; Choi, J.; Lee, J.; Yoon, S.; Kim, K.; Shin, J.; Suh, J.; Cheon, J. In Vivo Magnetic Resonance Detection of Cancer by Using Multifunctional Magnetic Nanocrystals. *J. Am. Chem. Soc.* **2005**, *127*, 12387−12391.

(7) Lartigue, L.; Hugounenq, P.; Alloyeau, D.; Clarke, S. P.; Le, M.; Levy, M.; Bazzi, R.; Brougham, D. F.; Wilhelm, C.; Gazeau, F. Cooperative Organization in Iron Oxide Multi-Core Nanoparticles Potentiates Their Efficiency as Heating Mediators and MRI Contrast Agents. *ACS Nano* **2012**, *6*, 10935−10949.

(8) Kim, B. H.; Lee, N.; Kim, H.; An, K.; Park, Y. I.; Choi, Y.; Shin, K.; Lee, Y.; Kwon, S. G.; Na, H. B.; Park, J.-G.; Ahn, T.-Y.; Kim, Y.-W.; Moon, H. K.; Choi, S. H.; Hyeon, T. Large-Scale Synthesis of Uniform and Extremely Small-Sized Iron Oxide Nanoparticles for High-Resolution T1Magnetic Resonance Imaging Contrast Agents. *J. Am. Chem. Soc.* **2011**, *133*, 12624−12631.

(9) Qiao, R.; Yang, C.; Gao, M. Superparamagnetic Iron Oxide Nanoparticles: From Preparations to In Vivo MRI Applications. *J. Mater. Chem.* **2009**, *19*, 6274−6293.

(10) Laurent, S.; Forge, D.; Port, M.; Roch, A.; Robic, C.; Elst, L.; Vander; Müller, R. N. Magnetic Iron Oxide Nanoparticles: Synthesis, Stabilization, Vectorization, Physicochemical Characterizations, and Biological Applications. *Chem. Rev.* **2008**, *108*, 2064−2110.

(11) Gupta, K. A.; Gupta, M. Synthesis and Surface Engineering of Iron Oxide Nanoparticles for Biomedical Applications. *Biomaterials* **2005**, *26*, 3995−4021.

(12) Sun, S.; Zeng, H. Size-Controlled Synthesis of Magnetite Nanoparticles. *J. Am. Chem. Soc.* **2002**, *124*, 8204−8205.

(13) Guardia, P.; Labarta, A.; Batlle, X. Tuning the Size, the Shape, and the Magnetic Properties of Iron Oxide Nanoparticles. *J. Phys. Chem. C* **2011**, *115*, 390−396.

(14) Hyeon, T.; Lee, S. S.; Park, J.; Chung, Y.; Na, H. B. Synthesis of Highly Crystalline and Monodisperse Maghemite Nanocrystallites without a Size-Selection Process. *J. Am. Chem. Soc.* **2001**, *123*, 12798−12801.

(15) Park, J.; An, K.; Hwang, Y.; Park, J.; Noh, H.; Kim, J.; Park, J.; Hwang, N.; Hyeon, T. Ultra-Large-Scale Syntheses of Monodisperse Nanocrystals. *Nat. Mater.* **2004**, *3*, 891−895.

(16) Jeong, U.; Teng, X.; Wang, Y.; Yang, H.; Xia, Y. Superparamagnetic Colloids: Controlled Synthesis and Niche Applications. *Adv. Mater.* **2007**, *19*, 33−60.

(17) Hu, B. F.; Wei, L.; Zhou, Z.; Ran, Y.; Li, Z.; Gao, M. Preparation of Biocompatible Magnetite Nanocrystals for In Vivo Magnetic Resonance Detection of Cancer. *Adv. Mater.* **2006**, *18*, 2553−2556.

(18) Wan, J.; Cai, W.; Meng, X.; Liu, E. Monodisperse Water-Soluble Magnetite Nanoparticles Prepared by Polyol Process for High-Performance Magnetic Resonance Imaging. *Chem. Commun.* **2007**, *4*, 5004−5006.

(19) Hu, F.; MacRenaris, K. W.; Waters, E. A.; Liang, T.; Schultz-Sikma, E. A.; Eckermann, A. L.; Meade, T. J. Ultrasmall, Water-Soluble Magnetite Nanoparticles with High Relaxivity for Magnetic Resonance Imaging. *J. Phys. Chem. C* **2009**, *113*, 20855−20860.

(20) Jia, X.; Chen, D.; Jiao, X.; Zhai, S. Environmentally-Friendly Preparation of Water-Dispersible Magnetite Nanoparticles. *Chem. Commun.* **2009**, *3*, 968−970.

(21) Lu, A.-H.; Salabas, E. L.; Schüth, F. Magnetic Nanoparticles: Synthesis, Protection, Functionalization, and Application. *Angew. Chem., Int. Ed. Engl.* **2007**, *46*, 1222−1244.

(22) Guardia, P.; Pérez-Juste, J.; Labarta, A.; Batlle, X.; Liz-Marzán, L. M. Heating Rate Influence on the Synthesis of Iron Oxide Nanoparticles: The Case of Decanoic Acid. *Chem. Commun.* **2010**, *46*, 6108−6110.

(23) Sun, S.; Zeng, H. Size-Controlled Synthesis of Magnetite Nanoparticles. *J. Am. Chem. Soc.* **2002**, *124*, 8204−8205.

(24) Park, J.; Lee, E.; Hwang, N.-M.; Kang, M.; Kim, S. C.; Hwang, Y.; Park, J.-G.; Noh, H.-J.; Kim, J.-Y.; Park, J.-H.; et al. One-Nanometer-Scale Size-Controlled Synthesis of Monodisperse Magnetic Iron Oxide Nanaoparticles. *Angew. Chem., Int. Ed. Engl.* **2005**, *44*, 2872−2877.

DOI: 10.1021/am508404t
ACS Appl. Mater. Interfaces 2015, 7, 6530−6540

(25) Cheng, D.; Hong, G.; Wang, W.; Yuan, R.; Ai, H.; Sen, J.; Liang, B.; Gao, J.; Shuai, X. Nonclustered Magnetite Nanoparticle Encapsulated Biodegradable Polymeric Micelles with Enhanced Properties for in Vivo Tumor Imaging. *J. Mater. Chem.* **2011**, *21*, 4796−4804.
(26) Hofmann, A.; Thierbach, S.; Semisch, A.; Hartwig, A.; Taupitz, M.; Eckart, R.; Graf, C. Highly Monodisperse Water-Dispersable Iron Oxide Nanoparticles for Biomedical Applications. *J. Mater. Chem.* **2010**, *20*, 7842−7853.
(27) Qin, B. J.; Laurent, S.; Jo, Y. S.; Roch, A.; Mikhaylova, M.; Bhujwalla, Z. M.; Muller, R. N.; Muhammed, M. A High-Performance Magnetic Resonance Imaging T2 Contrast Agent. *Adv. Mater.* **2007**, *19*, 1874−1878.
(28) Wang, Y.; Wong, J. F.; Teng, X.; Lin, X. Z.; Yang, H. "Pulling" Nanoparticles into Water: Phase Transfer of Oleic Acid Stabilized Monodisperse Nanoparticles into Aqueous Solutions of a-Cyclodextrin. *Nano Lett.* **2003**, *3*, 1555−1559.
(29) Xiao, L.; Li, J.; Brougham, D. F.; Fox, E. K.; Feliu, N.; Bushmelev, A.; Schmidt, A.; Mertens, N.; Kiessling, F.; Valldor, M.; et al. Water-Soluble Superparamagnetic Magnetite Nanoparticles with Biocompatible Coating for Enhanced Magnetic Resonance Imaging. *ACS Nano* **2011**, *5*, 6315−6324.
(30) Xiao, L. *Green Nanochemistry: Synthesis and Surface Functionalization of Tin and Iron Oxide Nanoparticles for Gas Sensing, Imaging (MRI) and Cellular Uptake Applications*; Verlag: Munich, 2012
(31) Zaveri, N. T. Green Tea and Its Polyphenolic Catechins: Medicinal Uses in Cancer and Noncancer Applications. *Life Sci.* **2006**, *78*, 2073−2080.
(32) Abd-ElSalam, H. H.; Al-Ghobashy, M. A.; Zaazaa, H. E.; Ibrahim, M. A. Stability of Catechins in Green Tea Nutraceutical Products: Application of Solid Phase Extraction—Thin Layer Chromatography Densitometry. *Food Chem.* **2014**, *156*, 94−99.
(33) Wu, Y.; Huang, F.; Lin, Y. Fluorescent Detection of Lead in Environmental Water and Urine Samples Using Enzyme Mimics of Catechin-Synthesized Au Nanoparticles. *ACS Appl. Mater. Interfaces* **2013**, *5*, 1503−1509.
(34) Manea, A.; Vasile, B. S.; Meghea, A. Antioxidant and Antimicrobial Activities of Green Tea Extract Loaded into Nanostructured Lipid Carriers. *C. R. Chim.* **2014**, *17*, 331−341.
(35) Liao, R.; Tang, Z.; Lei, Y.; Guo, B. Polyphenol-Reduced Graphene Oxide: Mechanism and Derivatization. *J. Phys. Chem. C* **2011**, *115*, 20740−20746.
(36) Nadagouda, M. N.; Varma, R. S. Green Synthesis of Silver and Palladium Nanoparticles at Room Temperature Using Coffee and Tea Extract. *Green Chem.* **2008**, *10*, 859−862.
(37) Hoag, G. E.; Collins, J. B.; Holcomb, J. L.; Hoag, J. R.; Nadagouda, N.; Varma, R. S. Degradation of Bromothymol Blue by "Greener" Nano-Scale Zero-Valent Iron Synthesized Using Tea Polyphenols. *J. Mater. Chem.* **2009**, *19*, 8671−8677.
(38) Moulton, M. C.; Braydich-Stolle, L. K.; Nadagouda, M. N.; Kunzelman, S.; Hussain, S. M.; Varma, R. S. Synthesis, Characterization and Biocompatibility of "Green" Synthesized Silver Nanoparticles Using Tea Polyphenols. *Nanoscale* **2010**, *2*, 763−770.
(39) Wang, Y.; Shi, Z.; Yin, J. Facile Synthesis of Soluble Graphene via a Green Reduction of Graphene Oxide in Tea Solution and Its Biocomposites. *ACS Appl. Mater. Interfaces* **2011**, *3*, 1127−1133.
(40) Tejero, I.; Gonzalez-Garcia, N.; Gonzales-Lafont, A.; Lluch, J. M. Tunneling in Green Tea: Understanding the Antioxidant Activity of Catechol-Containing Compounds. A Variational Transition-State Theory Study. *J. Am. Chem. Soc.* **2007**, 5846−5854.
(41) Huang, X.; Wu, H.; Shi, B. One-Step, Size-Controlled Synthesis of Gold Nanoparticles at Room Temperature Using Plant Tannin. *Green Chem.* **2010**, *12*, 395−399.
(42) Quideau, S.; Deffieux, D.; Douat-Casassus, C.; Pouysøgu, L. Natural Products Plant Polyphenols: Chemical Properties, Biological Activities, and Synthesis. *Angew. Chem., Int. Ed.* **2011**, *50*, 586−621.
(43) Krais, A.; Wortmann, L.; Hermanns, L.; Feliu, N.; Vather, M.; Stucky, S.; Mathur, S.; Fadeel, B. Targeted Uptake of Folic Acid-Functionalized Iron-Oxide Nanoparticles by Overian Cancer Cells in the Presence but not in the Absence of Serum. *Nanomedicine* **2014**, *10*, 1421−1431.
(44) Wortmann, L.; Ilyas, S.; Niznansky, D.; Valldor, M.; Arroub, K.; Berger, N.; Rahme, K.; Holmes, J.; Mathur, S. Bioconjugated Iron Oxide Nanocubes: Synthesis, Functionalization and Vectorization. *ACS Appl. Mater. Interfaces* **2014**, *6*, 16631−16642.
(45) El-Gamel, N.; Wortmann, L.; Arroub, K.; Mathur, S. SiO_2@Fe_2O_3 Core-Shell Nanoparticles for Covalent Immobilization and Release of Sparfloxacin Drug. *Chem. Commun.* **2011**, *47*, 10076−10078.
(46) Patterson, A. L. The Scherrer Formula for X-Ray Particle Size Determination. *Phys. Rev.* **1939**, *56*, 978−982.
(47) Bors, W.; Michel, C.; Stettmaier, K. Electron Paramagnetic Resonance Studies of Radical Species of Proanthocyanidins and Gallate Esters. *Arch. Biochem. Biophys.* **2000**, *374*, 347−355.
(48) Lu, X.; Niu, M.; Qiao, R.; Gao, M. Superdispersible PVP-Coated Fe_3O_4 Nanocrystals Prepared by a "One-Pot" Reaction. *J. Phys. Chem. B* **2008**, *112*, 14390−14394.
(49) Li, B. Z.; Wei, L.; Gao, M.; Lei, H. One-Pot Reaction to Synthesize Biocompatible Magnetite Nanoparticles. *Adv. Mater.* **2005**, *17*, 1001−1005.
(50) Li, Z.; Chen, H.; Bao, H.; Gao, M. One-Pot Reaction to Synthesize Water-Soluble Magnetite Nanocrystals. *Chem. Mater.* **2004**, *16*, 12−14.
(51) Hansen, M. F.; Morup, S. Estimation of Blocking Temperatures from ZFC/FC Curves. *J. Magn. Magn. Mater.* **1999**, *203*, 214−216.
(52) García-Otero, J.; Porto, M.; Rivas, J.; Bunde, A. Influence of Dipolar Interaction on Magnetic Properties of Ultrafine Ferromagnetic Particles. *Phys. Rev. Lett.* **2000**, *84*, 167−170.
(53) Kechrakos, D.; Trohidou, K. N. Competition Between Dipolar and Exchange Interparticle Interactions in Magnetic Nanoparticle Films. *J. Magn. Magn. Mater.* **2003**, *262*, 107−110.
(54) Smart, J. S. The Néel Theory of Ferrimagnetism. *Am. J. Phys.* **1976**, 356.
(55) Wang, Y. J. Superparamagnetic Iron Oxide Based MRI Contrast Agents: Current Status of Clinical Application. *Quant. Imaging Med. Surg.* **2011**, *1*, 35−40.

DOI: 10.1021/am508404t
ACS Appl. Mater. Interfaces 2015, 7, 6530−6540